

Article

Post-Synthetically Treated ERI and SSZ-13 Zeolites Modified with Copper as Catalysts for NH₃-SCR-DeNO_x

Alejandro Mollá Robles ¹, Gabriele Deplano ², Kinga Góra-Marek ³, Marek Rotko ⁴, Anna Wach ⁵, Muhammad Fernadi Lukman ⁶, Marko Bertmer ⁶, Matteo Signorile ², Silvia Bordiga ², Andreas Pöppel ⁶, Roger Gläser ¹ and Magdalena Jabłońska ^{1,*}

¹ Institute of Chemical Technology, Universität Leipzig, Linnéstr. 3, 04103 Leipzig, Germany; roger.glaeser@uni-leipzig.de (R.G.)

² Department of Chemistry, NIS Center and INSTM Reference Center, University of Turin, Via P. Giuria 7, 10125 Turin, Italy; gabriele.deplano@unito.it (G.D.); matteo.signorile@unito.it (M.S.); silvia.bordiga@unito.it (S.B.)

³ Faculty of Chemistry, Jagiellonian University in Krakow, Gronostajowa 2, 30-387 Krakow, Poland

⁴ Department of Chemical Technology, Institute of Chemical Sciences, Faculty of Chemistry, Maria Curie-Skłodowska University, 3 Maria Curie-Skłodowska Sq., 20-031 Lublin, Poland

⁵ Paul Scherrer Institute, 5232 Villigen, Switzerland; anna.wach@uj.edu.pl

⁶ Felix Bloch Institute for Solid State Physics, Universität Leipzig, Linnéstr. 5, 04103 Leipzig, Germany; muhammad_fernadi.lukman@uni-leipzig.de (M.F.L.); bertmer@physik.uni-leipzig.de (M.B.)

* Correspondence: magdalena.jablonska@uni-leipzig.de

Abstract: ERI and SSZ-13 were subjected to post-synthetic treatments (depending on the zeolite topology) to create micro-/mesoporous materials. The results in terms of NH₃-SCR-DeNO_x show that the applied treatments improved the catalytic activity of the Cu-containing ERI-based materials; however, the NO conversion did not vary for the different materials treated with NaOH or NaOH/HNO₃. For the micro-/mesoporous Cu-containing SSZ-13, a lower NO conversion in NH₃-SCR-DeNO_x was observed. Thus, our findings challenge the current paradigm of enhanced activity of micro-/mesoporous catalysts in NH₃-SCR-DeNO_x. The modification of the supports results in the presence of different amounts and kinds of copper species (especially isolated Cu²⁺ and aggregated Cu species) in the case of ERI- and SSZ-13-based samples. The present copper species further differentiate the formation of reactive reaction intermediates. Our studies show that besides the μ-η², η²-peroxo dicopper(II) complexes (verified by in situ DR UV-Vis spectroscopy), copper nitrates (evidenced by in situ FT-IR spectroscopy) also act as reactive intermediates in these catalytic systems.

Keywords: ERI; SSZ-13; copper species; NH₃-SCR-DeNO_x



Citation: Robles, A.M.; Deplano, G.; Góra-Marek, K.; Rotko, M.; Wach, A.; Lukman, M.F.; Bertmer, M.; Signorile, M.; Bordiga, S.; Pöppel, A.; et al. Post-Synthetically Treated ERI and SSZ-13 Zeolites Modified with Copper as Catalysts for NH₃-SCR-DeNO_x. *Catalysts* **2024**, *14*, 457. <https://doi.org/10.3390/catal14070457>

Academic Editor: Antonio Eduardo Palomares

Received: 18 June 2024
Revised: 9 July 2024
Accepted: 13 July 2024
Published: 16 July 2024



Copyright: © 2024 by the authors. Licensee MDPI, Basel, Switzerland. This article is an open access article distributed under the terms and conditions of the Creative Commons Attribution (CC BY) license (<https://creativecommons.org/licenses/by/4.0/>).

1. Introduction

The selective catalytic reduction of nitrogen oxides with ammonia (NH₃-SCR-DeNO_x) is widely applied as an emission control process to eliminate NO_x from diesel engines as well as power plants. NH₃-SCR-DeNO_x technology, using a commercial V₂O₅-WO₃/TiO₂ (abbreviated as VWTi) catalyst, has proved to be very effective for removing the NO_x in flue gas from stationary sources. However, SCR catalysts often deactivate when exposed to sulfurated and moist conditions in waste incineration power plants [1,2]. Also, in the oxidizing environment of diesel engines, high-temperature excursions in the presence of water vapor can lead to the deactivation of catalysts, such as the dealumination of zeolite-based materials [3]. So far, many catalysts have been investigated in NH₃-SCR-DeNO_x, including vanadium pentoxide-based catalysts, transition metal-exchanged zeolites (e.g., Cu-Y or Cu-SSZ-13), and hybrid catalysts (e.g., Ce-Zn mixed oxides with Fe-ZSM-5 or Zn-Ti mixed oxides with Cu-SSZ-13, etc.) [4–6]. Furthermore, besides catalysts based on SSZ-13 or ZSM-5, Cu-containing ERI has revealed enhanced catalytic properties in NH₃-SCR-DeNO_x. For example, Zhu et al. [7] proved that their fast-synthesized Cu-containing ERI

achieved a catalytic activity comparable to the commercial Cu-SSZ-13. Moreover, Sultana et al. [8] reported that Cu-ERI catalysts showed similar catalytic activity to Cu-ZSM-5, albeit with higher resistance against decane poisoning. Some researchers claimed that the activity and N₂ selectivity in both NH₃-SCR-DeNO_x and the selective catalytic oxidation of ammonia (NH₃-SCO) have been enhanced for micro-/mesoporous materials (e.g., Cu-ZSM-5, Cu-SAPO-34, Fe-ZSM-5) [9–11]. For example, Oord et al. [12] and Wu et al. [13] applied the post-synthetic modification of SSZ-13 with an aqueous solution of NaOH. They both found that the catalytic activity and N₂ selectivity can be improved for Cu-SSZ-13 (with the support treated with 0.1 M solution). Otherwise, the post-synthetic modification above 0.1 M led to a drop in the catalytic properties of the materials. On the other hand, Jabłońska et al. found that the mesopores introduced into Cu-containing zeolite ZSM-5 [14] or Y [15] catalysts do not play any direct role in the activity of the NH₃-SCR-DeNO_x. Although Tekla et al. [16] introduced mesoporosity into erionite using both acid- and alkali-leaching treatments, such materials have not been investigated in NH₃-SCR-DeNO_x or NH₃-SCO. Given the discrepancies mentioned above, further studies of micro-/mesoporous materials are required to understand the relationship between mesoporosity, catalytic activity, and N₂ selectivity in NH₃-SCR-DeNO_x. Thus, ERI and SSZ-13 zeolites were subjected to different post-synthetic treatments, depending on the zeolite topology, including treatment with NaOH or sequential treatment with HNO₃, followed by treatment with NaOH. The structure, texture, elemental analysis, and acidic properties of the copper-containing zeolites were characterized by X-ray diffraction (XRD), solid-state nuclear magnetic resonance (NMR), N₂ sorption, inductively coupled plasma optical emission spectroscopy (ICP-OES), and temperature-programmed desorption of NH₃ (NH₃-TPD). The nature of the copper species was investigated by temperature-programmed reduction of H₂ (H₂-TPR), as well as by diffuse reflectance UV-Vis (DR UV-Vis), extended X-ray absorption fine structure (EXAFS), and electron paramagnetic resonance (EPR) spectroscopy. The activity and N₂ selectivity were evaluated via NH₃-SCR-DeNO_x ($4 \text{ NH}_3 + 4 \text{ NO} + \text{O}_2 \rightarrow 4 \text{ N}_2 + 6 \text{ H}_2\text{O}$) and NH₃-SCO ($4 \text{ NH}_3 + 3 \text{ O}_2 \rightarrow 2 \text{ N}_2 + 6 \text{ H}_2\text{O}$) for the Cu form of conventional zeolites, post-synthetically treated SSZ-13, and especially, ERI for the first time in the literature. Furthermore, the reaction pathways were investigated through in situ Fourier transform infrared (FT-IR) and DR UV-Vis spectroscopy and temperature-programmed studies with the ¹⁸O₂ isotope over both zeolite topologies to deepen our understanding of the reactive reaction intermediates, and thus, maximize their potential in industrial applications.

2. Results and Discussion

2.1. Structural and Textural Properties

The commercial zeolites ERI (Clariant, $n(\text{Si})/n(\text{Al}) = 3.5$) and SSZ-13 (Clariant, $n(\text{Si})/n(\text{Al}) = 6.5$) were post-synthetically modified according to previously reported protocols optimized for any specific zeotype [12,14–16]. Table 1 summarizes the applied modifications.

Table 1. Sample labels and treatment conditions.

Sample	Applied Treatment
ERI_HNO ₃ _NaOH/0.5_0.5	0.3 M HNO ₃ at 65 °C for 0.5 h followed by 0.2 M NaOH at 65 °C for 0.5 h
ERI_HNO ₃ _NaOH/0.5_2	0.3 M HNO ₃ at 65 °C for 0.5 h followed by 0.2 M NaOH at 65 °C for 2 h
ERI_NaOH/2	0.2 M NaOH at 65 °C for 2 h
SSZ-13_NaOH/0.5	0.2 M NaOH at 65 °C for 0.5 h
SSZ-13_NaOH/2	0.2 M NaOH at 65 °C for 2 h

Figure 1 shows the XRD patterns of the parent ERI and SSZ-13, as well as their Cu-containing forms. The XRD patterns of the commercial calcined zeolites are typical of the pure erionite (ERI topology) and SSZ-13 (CHA) structure, as reported before [12,14,16]. The structure of the zeolites is preserved after the post-synthetic treatment (Figure S1) as well

as after the ion exchange and subsequent calcination. Furthermore, no peaks at $2\theta = 35.6^\circ$ and 38.7° corresponding to copper phases [17] are detected in the diffractograms of the Cu-containing samples, indicating the crystal sizes of the copper species to be below the XRD analysis detection limit.

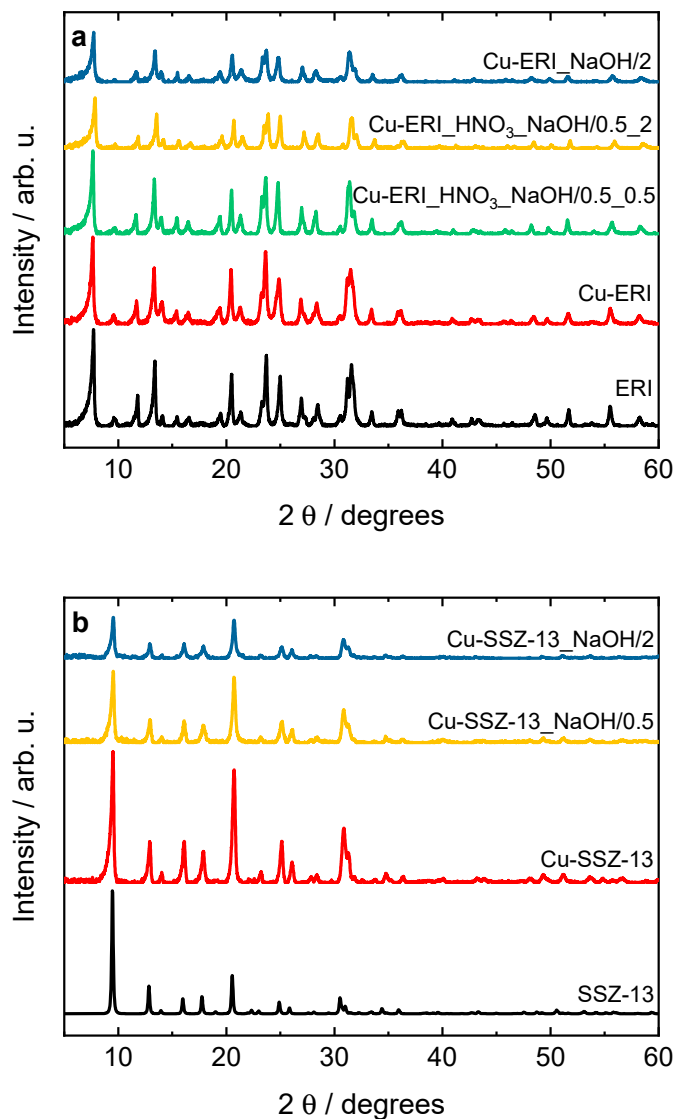


Figure 1. XRD patterns of the (a) ERI and (b) SSZ-13 samples and their Cu-containing forms (sample labels as in Table 2).

Table 2. The elemental analysis results of the ERI and SSZ-13 samples and their Cu-containing forms (ω_i : mass fractions).

Sample	$\omega_{Al}/wt. \%$	$\omega_{Si}/wt. \%$	$\omega_{Cu}/wt. \%$	$n(Si)/n(Al)$	$n(Cu)/n(Al)$
ERI	8.8	31.5	-	3.4	-
Cu-ERI	8.2	29.9	6.1	3.5	0.3
Cu-ERI_NaOH/2	7.9	23.7	3.7	2.9	0.2
Cu-ERI_HNO ₃ _NaOH/0.5_0.5	7.7	25.5	3.4	3.2	0.2
Cu-ERI_HNO ₃ _NaOH/0.5_2	7.6	21.5	3.1	2.7	0.2
SSZ-13	6.1	38.3	-	6.0	-
Cu-SSZ-13	5.8	36.2	4	6.0	0.3
Cu-SSZ-13_NaOH/0.5	6.6	24.6	3	3.6	0.2
Cu-SSZ-13_NaOH/2	6.7	24.2	3.3	3.5	0.2

Table 2 lists the results of the elemental analysis determined by ICP-OES. The measured $n(\text{Si})/n(\text{Al})$ ratio of the parent zeolites (i.e., ERI: 3.4, SSZ-13: 6.0) is close to the one reported by the supplier (i.e., ERI: 3.5, SSZ-13: 6.5). However, after the post-synthetic treatment, the $n(\text{Si})/n(\text{Al})$ ratios decrease in the series of ERI- and SSZ-13-based materials. For example, for Cu-ERI_HNO₃_NaOH/0.5_0.5 and Cu-ERI_HNO₃_NaOH/0.5_2, the time during the alkali leaching has a more substantial influence on the $n(\text{Si})/n(\text{Al})$ ratios than the application of an acid leaching before the alkali one. For the SSZ-13-based samples, the $n(\text{Si})/n(\text{Al})$ ratios are reduced by ca. 40% after the alkali treatments, although the treatment time (i.e., 0.5 or 2 h) does not influence the decrease in the silica content. Overall, the post-synthetic treatments of both the ERI- and SSZ-13-based samples can extract Si species from the framework and Al species to a lesser degree. In addition, the Cu weight loading does not significantly vary for the post-treated ERI or SSZ-13 samples.

Figure 2 and Figure S2 show the N₂ sorption isotherms of the parent ERI, SSZ-13 samples, and their Cu-containing forms, while Table 3 and Table S1 gather the results concerning the textural properties of the parent and post-modified forms of the ERI and SSZ-13 samples. The isotherms of the Cu-containing ERI-based samples (Figure 2a) can be categorized as type I isotherms [18], while the samples based on the post-modified ERI show a higher adsorbed volume of nitrogen, especially at $p/p_0^{-1} > 0.8$. These samples also present higher mesopore volume values than Cu-ERI (increase from 0.04 cm³ g⁻¹ to 0.05–0.10 cm³ g⁻¹, Table 3). The BJH pore width distribution (Figure 2c) shows mesopores in the broad range of up to 10 nm for both Cu-ERI_HNO₃_NaOH/0.5_0.5 and Cu-ERI_HNO₃_NaOH/0.5_2. The results align with the data reported by Tekla et al. [16] (on which the preparation steps were based), where minor changes in the type of the adsorption isotherm or pore width distribution profile were found between the different treatments of ERI-based samples. Cu-SSZ-13 also shows type I isotherms. However, after the post-synthetic treatments of the support, the isotherms of the related Cu-containing samples become a mixture of type I and type IV, with an H4 hysteresis loop, which is a typical trait of mesoporous materials [18] (Figure 2b). The adsorbed volume increases in the region of medium relative pressure, which could be related to the rise in the mesopore volume of these samples (increase from 0.03 cm³ g⁻¹ to 0.23–0.26 cm³ g⁻¹, Table 3). Furthermore, the pore width distribution results (Figure 2d) show an increase in the mesopores up to 35 nm independent of the treatment time of the SSZ-13 sample. In line with the studies of Sommer et al. [19] and Oord et al. [12], we also observed a decrease in the specific surface area of the post-modified Cu-containing SSZ-13 compared to the other topologies, i.e., ERI [16]. Such changes in the specific surface area arise due to the impact of the demetallation on the parent ERI and SSZ-13 samples.

Table 3. The results concerning the textural properties of ERI, SSZ-13, and their Cu-containing forms: specific surface area ($A_{\text{s(BET)}}$), micropore pore volume ($V_{\text{(MIC)}}$), mesopore pore volume ($V_{\text{(MES)}}$), total pore volume ($V_{\text{(TOT)}}$) and average pore width (d_{WP}).

Sample	$A_{\text{s(BET)}}$ /m ² g ⁻¹	$V_{\text{(MIC)}}$ /cm ³ g ⁻¹	$V_{\text{(MES)}}$ /cm ³ g ⁻¹	$V_{\text{(TOT)}}$ /cm ³ g ⁻¹	d_{WP} /nm
ERI	525	0.19	0.04	0.24	2.7
Cu-ERI	396	0.14	0.04	0.18	2.6
Cu-ERI_HNO ₃ _NaOH/0.5_0.5	466	0.17	0.10	0.27	3.9
Cu-ERI_HNO ₃ _NaOH/0.5_2	479	0.17	0.09	0.28	4.0
Cu-ERI_NaOH/2	467	0.18	0.05	0.23	2.7
SSZ-13	716	0.26	0.06	0.32	4.0
Cu-SSZ-13	672	0.25	0.03	0.28	3.2
Cu-SSZ-13_NaOH/0.5	526	0.14	0.23	0.37	4.9
Cu-SSZ-13_NaOH/2	560	0.13	0.26	0.39	4.8

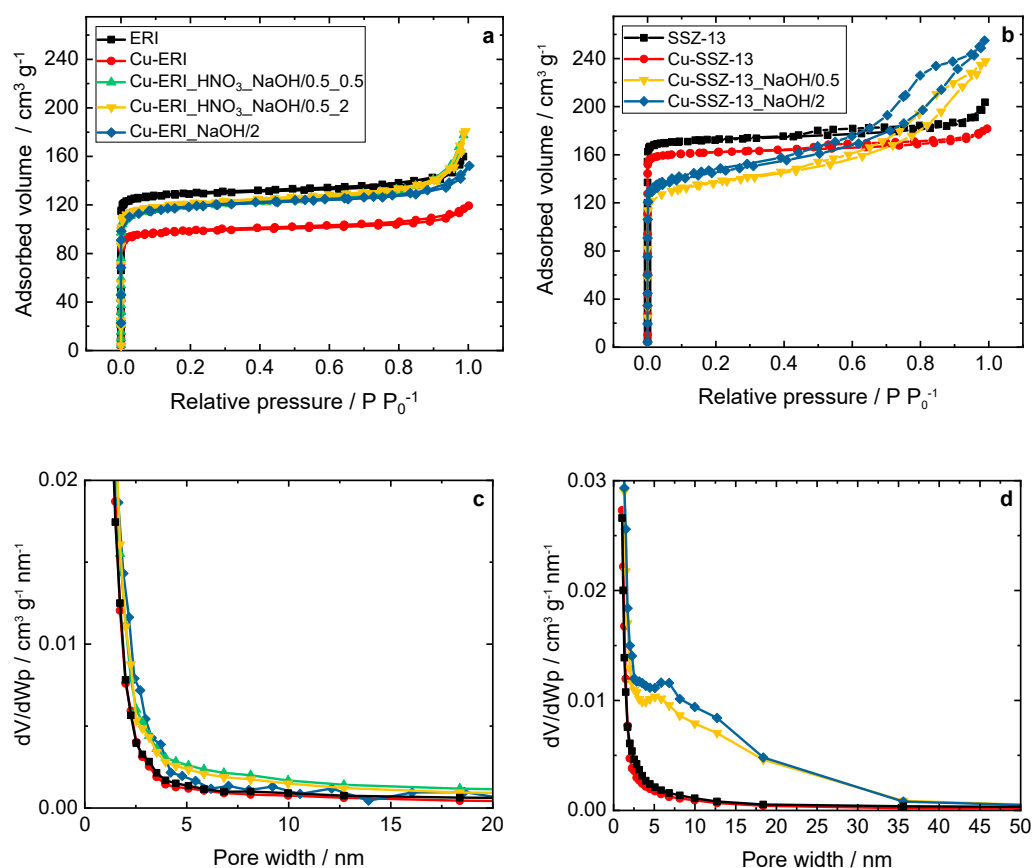


Figure 2. (a,b) N₂ sorption isotherms collected at $-196\text{ }^{\circ}\text{C}$ and (c,d) BJH pore width distribution of the ERI and SSZ-13 samples, and their Cu-containing forms; (a,c) and (b,d) sample labels are identical.

As the physico-chemical characterization revealed no significant contrast between the various applied post-modified ERI- and SSZ-13-based samples, we narrowed our studies to the deeper investigation of the copper form of leached ERI and SSZ-13 (under an aqueous solution of 0.2 M NaOH for 2 h). In order to investigate the influence of the post-synthetic treatment on the coordination of Si and Al atoms, we applied ²⁹Si and ²⁷Al solid-state NMR (Figure 3 and Figure S3a, Tables S2 and S3). Regarding Cu-ERI, four types of Si coordination are detected (Figure 3a), with the main coordination structure for Si(2Si,2Al) and Si(1Si,3Al) [20,21], encompassing 36.7% of the spectra's area (Figure S3). In Cu-ERI_NaOH/2, the main coordination structure changes to Si(4Si,0Al), indicating the substantial removal of Al species. Moreover, aluminum in the tetrahedral form (Al^{IV}) is observed as the main Al coordination for all the Cu-containing ERI samples, represented by the peak at about 62 ppm in the ²⁷Al NMR spectra (Figure 3c), together with a minor single of five-coordinated aluminum. The signal near 0 ppm present in Cu-ERI_NaOH/2 relates to the presence of extra-framework six-coordinated aluminum. For Cu-SSZ-13, mainly Si(3Si,1Al) and Si(4Si,0Al) appear [22] (Figure 3b), while for Cu-SSZ-13_NaOH/2, two other signals appear at about -94 ppm and -99 ppm related to Si(1Si,3Al) and Si(2Si,2Al), indicating the substantial removal of Si species in this sample (Figure S3a). The ²⁷Al NMR spectra (Figure 3d) of both Cu-containing SSZ-13 samples show the characteristic signal of tetrahedral aluminum species at about 60 ppm, together with a small amount of six-coordinated aluminum [23], while additionally for Cu-SSZ-13_NaOH/2, the presence of a signal near 37 ppm indicates the formation of a site with five-coordinated aluminum. Furthermore, the presence of these Al^{VI} forms in both Cu-ERI_NaOH/2 and Cu-SSZ-13_NaOH/2 contributes to the Lewis acidity. A schematic diagram of the coordination environment of Si and Al is shown in Figure S3b.

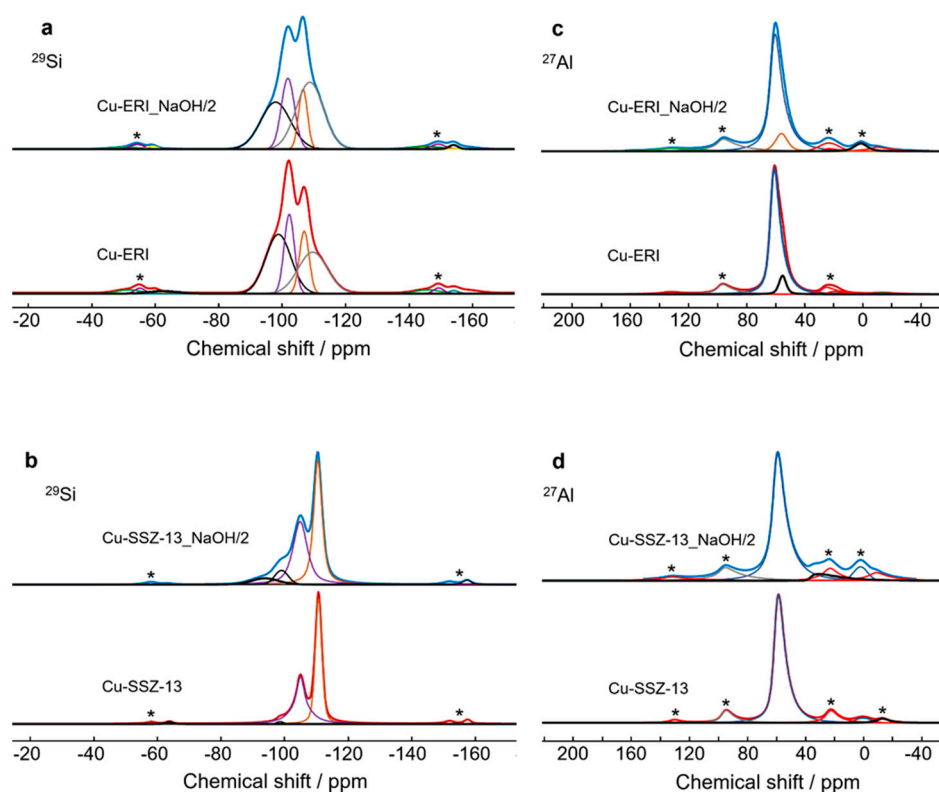


Figure 3. (a,b) ^{29}Si and (c,d) ^{27}Al NMR spectra of Cu-containing ERI and Cu-containing SSZ-13 samples; * indicates spinning sidebands.

Figure S4 shows the desorption NH_3 -TPD profiles of the Cu-containing ERI and SSZ-13 samples. According to the literature indications [24,25], the NH_3 desorption peak at around 300°C is characteristic of NH_3 adsorbed on the Lewis acid sites (L-NH_3), while the desorption peak centered at 440°C is assigned to NH_3 adsorbed as NH_4^+ on Brønsted sites (B-NH_4^+). Thus, our results reveal that the post-synthetic treatment of ERI and SSZ-13 zeolites effectively facilitates the formation of Lewis acid sites. Additionally, for Cu-ERI_NaOH/2, the peak maximum decreases toward lower temperatures, indicating their weaker strength.

2.2. Nature of Copper and Oxygen Species

The reducibility of the materials was investigated via H_2 -TPR measurements. Figure 4 shows the H_2 -TPR profiles of the Cu-containing ERI and SSZ-13 samples. For Cu-ERI, we can distinguish one peak centered at ca. 215°C , with a broad shoulder between 250 and 300°C . For Cu-ERI_NaOH/2, this reduction peak is shifted to a temperature higher by about 50°C . According to the literature indications [26,27], the first peak is associated with the reduction of Cu^{2+} species into Cu^+ and the second one with the reduction of Cu^+ species into Cu^0 . However, in the case of Cu-ERI, the first peak could also be related to the reduction of aggregated forms of the copper species that are more accessible for H_2 reduction (Figure S5a, Table S4). This statement is supported by the relatively high loading of copper in this sample (ICP-OES analysis, Table 2). Thus, both aggregated copper and isolated Cu^{2+} species are expected to be present in Cu-ERI. Otherwise, regarding the Cu-SSZ-13 sample, $[\text{Cu}(\text{OH})]^+$ (paired with Al located in eight-membered rings (8MRs)) and isolated Cu^{2+} (paired with two Al in six-membered rings (6MRs)) are reported as the main species present in this material. The $[\text{Cu}(\text{OH})]^+$ species in the 8MRs are more accessible to H_2 molecules than those in the 6MRs, which explains their higher reducibility compared to the other species [3]. Furthermore, the lower H_2 consumption of the first peak in Cu-SSZ-13_NaOH/2,

coupled with the lower Cu species content compared to Cu-SSZ-13 (Table 2), indicates a lower amount of $[\text{Cu}(\text{OH})]^+$ species in this sample (Figure S5b, Table S4).

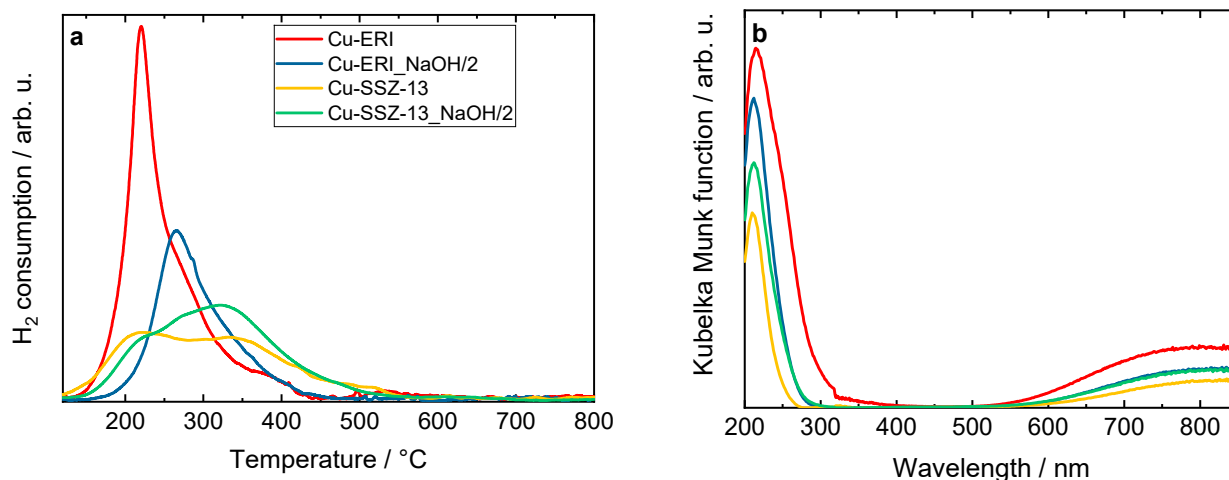


Figure 4. (a) H_2 -TPR profiles and (b) DR UV-Vis spectra of Cu-containing ERI and SSZ-13 samples; (a) and (b) sample labels are identical.

The DR UV-Vis profiles of the Cu-containing zeolites (Figure 4b) also vary depending on the zeolite topology or its post-synthetic modification. According to the literature [27–29], the oxygen-to-metal charge transfer between the lattice oxygen in the zeolite framework and the Cu^{2+} and Cu^+ species appears at around 200–260 nm. The bands in the 260–600 nm range proved the presence of the CuO species and $[\text{Cu-O-Cu}]^{2+}$ species. The absorption in the range of 600–850 nm is related to the d–d transitions of Cu^{2+} ions in pseudo-octahedral coordination (e.g., $\text{Cu}(\text{H}_2\text{O})_6^{2+}$). The higher copper content could explain the presence of aggregated copper species visible in Cu-ERI compared to the other materials.

Figure S6 depicts the EPR spectra of the hydrated Cu-containing zeolites, which can be interpreted as axially symmetric Cu^{2+} EPR signals with the characteristic hyperfine splitting pattern ($I = 3/2$) that slightly resolved at the parallel component ($B = 240\text{--}300$ mT), whereas the perpendicular component is not resolved. By performing spectral simulation, the hydrated spectra are characterized as anisotropic species (species K) with the spin Hamiltonian parameters of $g_{zz} = 2.380$ and $A_{zz} = 460$ MHz. However, in the case of the Cu-ERI and Cu-ERI_NaOH/2 samples, the presence of broader peaks at the parallel position of the EPR spectra indicates a higher degree of g_{zz} - and A_{zz} -strains for the Cu^{2+} complexes, thus translated into higher site heterogeneity [30]. Figure 5a,b show the analysis of the dehydrated Cu-containing zeolites, while the identified species can be classified according to Table S5. Table S6 is provided to demonstrate the contribution of several species to describe the experimental spectra. Based on the simulated spin Hamiltonian parameter of each experimental spectra, the assignment of the species can be deduced by comparing that parameter to the ones that are associated with fully hydrated Cu^{2+} , partially dehydrated Cu^{2+} , and fully dehydrated Cu^{2+} according to previous EPR studies of Cu-containing ERI and SSZ-13 [30–34]. The species K parameters match a fully hydrated Cu^{2+} (six-coordinated Cu^{2+} species with water ligand $[\text{Cu}(\text{H}_2\text{O})_6]^{2+}$). Species L corresponds to isolated Cu^{2+} species located at the 6MRs of the CHA structure. In addition, species M can be likewise assigned to the isolated Cu^{2+} species. Species O corresponds to four-coordinated square-planar-like structures, while species N is assigned to five-coordinated square-pyramid-like structures. Lastly, species P is related to isolated Cu^{2+} species that are suggested to have an octahedrally distorted geometry. In the case of the Cu-containing SSZ-13 samples, the spectral simulations can be derived from two different species. Species L is the dominant species, contributing 60% to the signal with the parameters $g_{zz} = 2.38$ and $A_{zz} = 420$ MHz, while the rest is attributed to species M, which can be observed with the parameters $g_{zz} = 2.33$ and $A_{zz} = 450$ MHz. For the Cu-containing ERI samples, species P and species N ($g_{zz} = 2.28$ and $A_{zz} = 545$ MHz) contribute to the spectra.

Although the dominant species in the Cu-ERI case is species P (90 %), for Cu-ERI_NaOH/2, the dominant species is species N (60 %). It can be concluded from the EPR data that the post-synthetic modifications conducted for the ERI- and SSZ-13-based samples tend to inflict a higher strain effect, which implies the relatively higher heterogeneity of the Cu^{2+} species distribution in the Cu-ERI_NaOH/2 and Cu-SSZ_NaOH/2 samples if compared to Cu-ERI and Cu-SSZ-13, respectively.

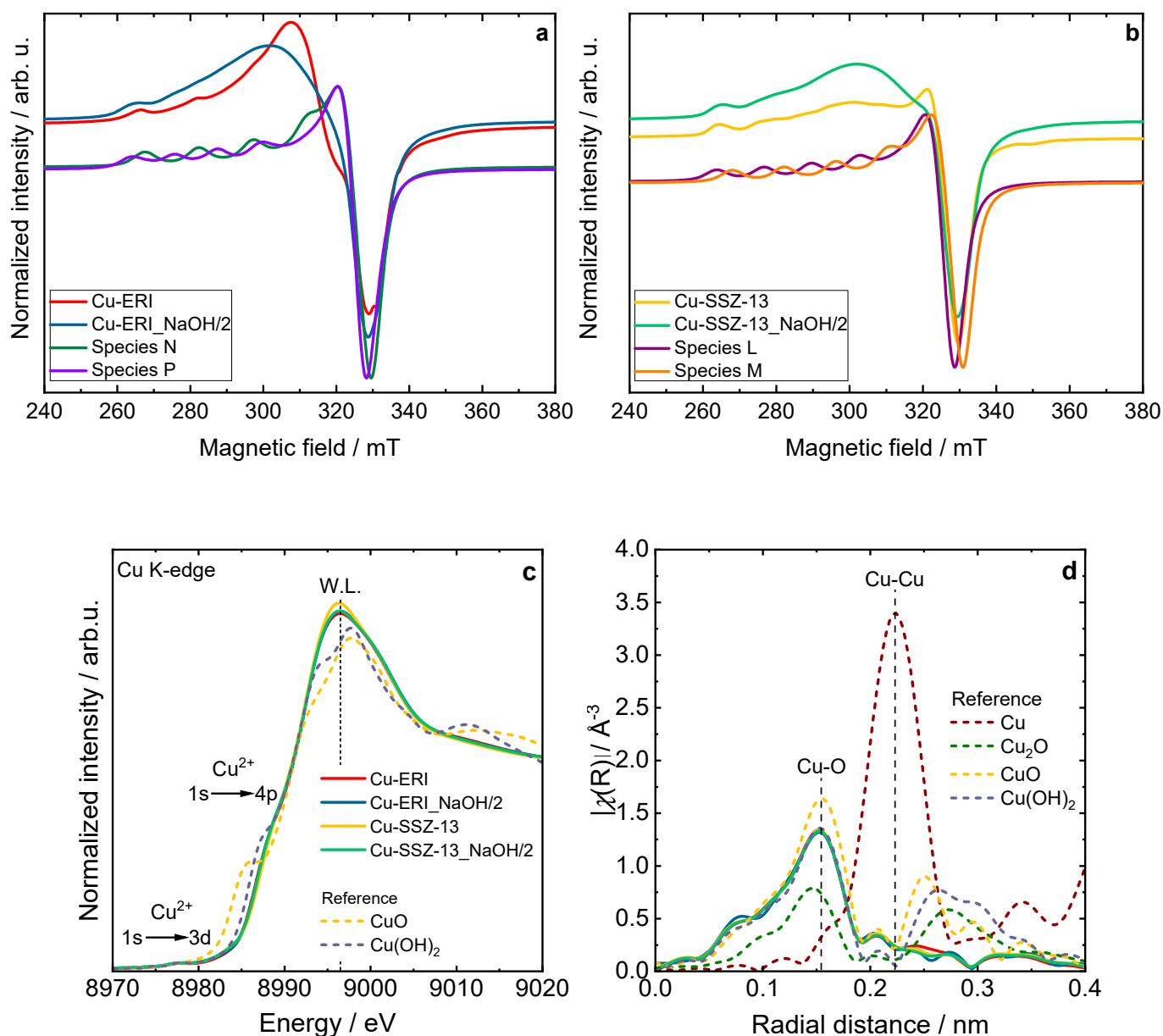


Figure 5. Experimental and simulated CW-EPR spectra of dehydrated (a) Cu-containing ERI and (b) SSZ-13 samples at the X-band, including the spectral simulation that adds the contribution of their respective species, (c) XANES spectra, and (d) EXAFS Fourier transforms of the Cu-containing zeolite samples compared with copper references; (c) and (d) sample labels are identical.

The shape and position of the XANES spectra revealed a Cu^{2+} oxidation state in all the Cu-containing zeolite samples (Figures 5c and S7). Namely, a weak pre-edge feature located at 8977.3–8977.5 eV and attributed to the $1s \rightarrow 3d$ quadrupole-allowed transition is not observed in the Cu^0 and Cu^+ species. Additionally, the position of the rising edge at about 8987.0 eV, corresponding to the dipole-allowed $1s \rightarrow 4p$ transitions, and the presence of a high-intensity white line at ca. 8996.4 eV, is characteristic of Cu^{2+} species in a highly

coordinated form, with a combination of water, framework oxygen, and OH groups in a coordination sphere [35,36].

The corresponding Fourier transform (FT) of the extended X-ray absorption fine structure (EXAFS) spectra for the Cu-containing zeolite samples and reference samples are presented in Figure 5d. As shown, the spectra of the Cu species in the zeolites correspond the most with the structure of cupric hydroxide. The spectra of all the synthesized samples exhibit an intense peak at 0.15 nm in the R-space, associated with backscattering from the oxygen atoms bonded directly to the copper atoms (Cu-O distances in the first coordination shell). Typically, features above 0.2 nm arise from Cu-Cu scattering (e.g., 0.22 nm in metallic Cu) and the second-shell Cu-O single scattering. The low-intensity second-shell peak at 0.205 nm, observed in all the zeolite samples, is attributed to the $[\text{Cu}(\text{H}_2\text{O})_6]^{2+}$ [37,38]. Nevertheless, the FT EXAFS spectra did not show a defined higher coordination shell (the absence of the distinct Cu-Cu contribution above 0.255 nm). This suggests the lack of long-range ordering of the copper sites in the studied zeolite samples [35].

It should be noted that there are no significant differences in the XANES and FT EXAFS spectra profiles between all the Cu-containing zeolite samples. The collected data confirm the formation of hydrated Cu^{2+} sites in the zeolites, as reported previously in the broad literature on XAS studies of the untreated hydrated Cu sites in metal-exchanged zeolites [35,37,38]. Recent studies suggest a dynamic equilibrium between Cu^{2+} sites six-, five- and even four-coordinated to O atoms from H_2O molecules [39,40]. Figure 6 and Figure S8 present the results of the temperature-programmed isotopic exchange (TPIE) studies carried out over the Cu-containing ERI and SSZ-13 samples. However, among the evaluated samples for only Cu-ERI, the TPIE results show that oxygen from the lattice of the metal oxide catalysts is exchanged with oxygen ($^{18}\text{O}_2$) from the gas phase. These results confirm that oxygen mobility is not decisive in the NH_3 -SCR-DeNO_x over these catalytic systems (Figure 7a).

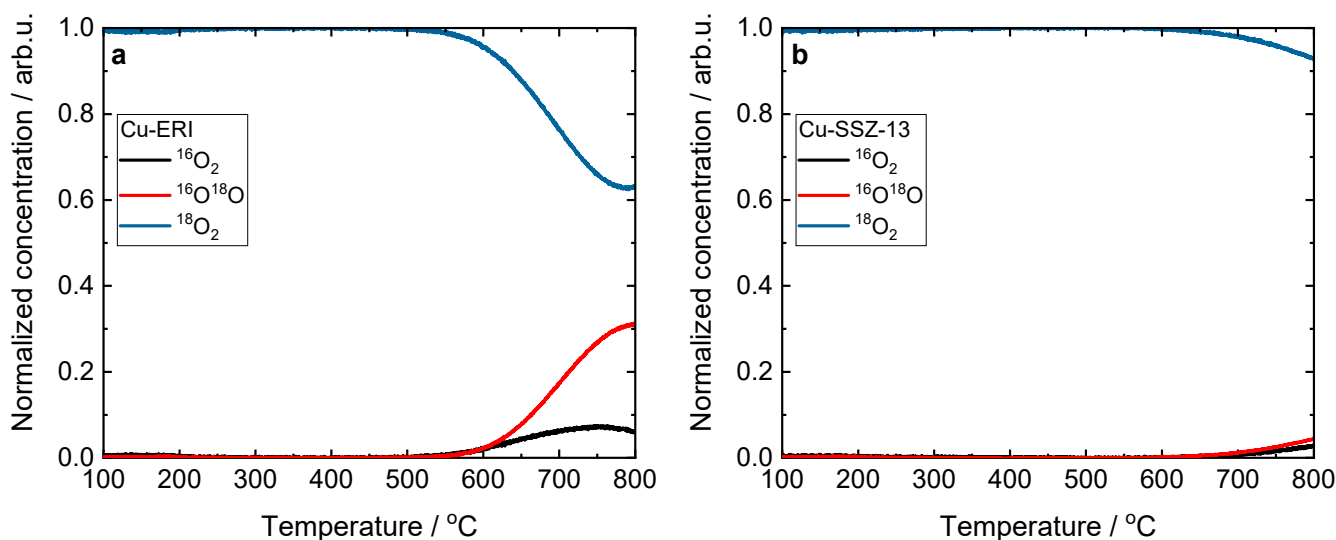


Figure 6. Results of the TPIE experiment obtained for (a) Cu-ERI and (b) Cu-SSZ-13.

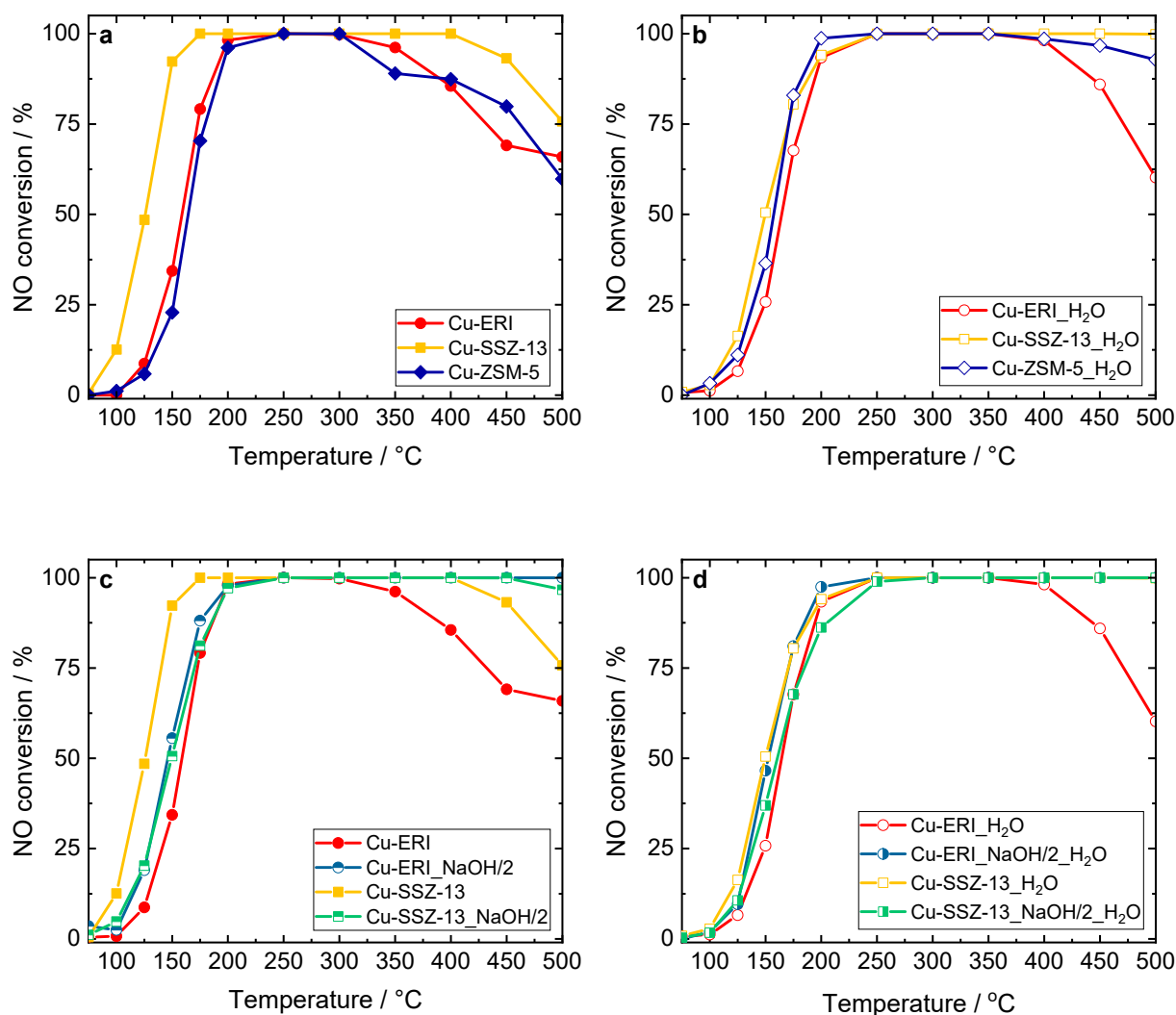


Figure 7. NO conversion of the Cu-containing ERI, SSZ-13, and ZSM-5 samples: (a,c) without H₂O in the feed, and (b,d) in the presence of H₂O in the feed. Reaction conditions: $m_K = 0.1$ g, $c(\text{NO}) = 0.05$ vol.%, $c(\text{NH}_3) = 0.0575$ vol.%, $c(\text{O}_2) = 4$ vol.%, ($c(\text{H}_2\text{O}) = 5$ vol.% when used), He balance, $F_{\text{TOT}} = 120$ ml min⁻¹, GHSV = 30,000 h⁻¹.

2.3. Catalytic Investigations

Figures 7, S9 and S10 present the results of the catalytic experiments for *standard* NH₃-SCR-DeNO_x, thus involving the reduction of NO with ammonia in the presence of excess oxygen with N₂ and water vapor formation. Among the different topologies applied, the highest NO conversion (without H₂O and in its presence in the feed) was achieved over Cu-containing SSZ-13 rather than Cu-ERI or Cu-ZSM-5 (Figure 7a,b). Cu-ZSM-5 was investigated for comparison and was fully characterized in our previous studies [14]. Similarly, other authors reported transition-metal-containing SSZ-13 to be more active than other zeolite-based catalysts [41]. Furthermore, the catalytic activity in NH₃-SCR-DeNO_x varied depending on the applied post-synthetic modification of the zeolites. For example, Cu-ERI_HNO₃_NaOH/0.5_0.5 and both Cu-ERI_NaOH/2 and Cu-ERI_HNO₃_NaOH/0.5_2 reach complete conversion up to 400–500 °C (Figure S9a). Furthermore, Cu-ERI_NaOH/2 reaches the highest NO conversion (between 250 and 500 °C) in the presence of 5 vol.-% H₂O. The significantly higher amount of aggregated copper species in Cu-ERI led to a drop in conversion above 350–400 °C due to the side reaction of NH₃ oxidation (NH₃-SCO). Indeed, our separate studies of ammonia oxidation revealed enhanced NH₃ conversion over Cu-ERI (Figure S10b). Furthermore, the lower

NH₃ conversion over Cu-ERI_NaOH/2 compared to Cu-ERI is supported by the H₂-TPR data, which reveal a lower amount of aggregated copper species in the first material. Only N₂ was identified among all the N-containing products in the NH₃-SCR-DeNO_x and NH₃-SCO over applied ERI-based catalysts.

In the Cu-containing SSZ-13-based catalysts, Cu-SSZ-13 shows higher NO conversion below 200 °C due to a higher content of highly reducible [Cu(OH)]⁺ species in this sample compared to the other samples. However, above 400 °C, the NO conversion decreases significantly compared to the other materials, again due to the side reaction of NH₃ oxidation (Figure S10b). Again, N₂ was the only detected product in NH₃-SCR-DeNO_x and NH₃-SCO over this series of samples. According to several reports [12,13,42], SSZ-13 is predominantly treated with an aqueous solution of 0.1 M NaOH (as an optimum solution between 0.05 and 0.3 M). Studies by Oord et al. [12] and further by Wu et al. [13] proved Cu-containing SSZ-13 with such a post-modified support to be the most active catalyst. Thus, to better compare our samples with the reported ones, we repeated the same post-synthetic modification of SSZ-13, with the preparation method for the catalyst as reported above [12,13], i.e., post-synthetic modification of SSZ-13 in a 0.1 M aqueous solution of NaOH. However, in our case, the activity of the respective catalyst was lower compared to Cu-SSZ-13 (Figure S10a). Still, it should be noted that the *n*(Si)/*n*(Al) ratio (12 and 17.8 versus 6 in our case), and thus the Cu species content (1.1 and 2.55 versus 3.3 wt.% of Cu in our case), as well as the related Cu species distribution, varied among our materials and the ones in the above-reported literature. For these reasons, the comparison is not straightforward. Thus, our following studies will constitute an investigation of micro-/mesoporous SSZ-13 with different *n*(Si)/*n*(Al) ratios.

In the case of chabazite-based catalysts, which possess a small cage aperture of 0.38 nm, the development of the mesopores is frequently assigned to overcoming the diffusion limitations (caused by the presence of micropores) and to enhancing the accessibility of the catalytically active centers. The determined activation energies, the Thiele modulus, and the effectiveness factor allow for a more direct assessment of the presence of diffusion limitations in the mesoporous zeolite-based catalysts compared to conventional reference materials. The reported activation energies of the Cu-containing ERI and SSZ-13 samples are 53 and 70–80 kJ mol⁻¹, respectively [7,43,44]. Interestingly, Zhang et al. [42] investigated core-shell-structured catalysts composed of an ordered mesoporous aluminosilicate (MAS) shell and a mesopore-containing Cu-SSZ-13 (prepared using the NaOH solution) core. In comparison with conventional Cu-SSZ-13, the meso-CuSSZ-13@MAS catalyst showed enhanced NO_x conversion due to an increase in the amount of isolated Cu²⁺ ions (based on H₂-TPR and NH₃-TPD analyses) and fewer pore diffusion limitations (based on the activation energy calculations). They reported that the introduction of mesoporosity into the system resulted in a higher activation energy than the conventional Cu-SSZ-13, which indicated a reduction in the pore diffusion limitations. In our case, we found 75 and 92 kJ mol⁻¹ for Cu-ERI and Cu-ERI_NaOH/2, as well as 77 and 70 kJ mol⁻¹ for Cu-SSZ-13 and Cu-SSZ-13_NaOH/2 for NH₃-SCR-DeNO_x without H₂O in the feed. However, the role of the formed mesopores in overcoming the diffusion limitations in NH₃-SCR-DeNO_x and NH₃-SCO is not excluded.

3. In Situ Spectroscopic Studies

When exposed to molecules with strong basicity (e.g., NH₃, H₂O), isolated Cu species are pulled away from their original position and migrate within the zeolite cages [45]. This reaction-driven dynamic Cu motion reflects the low-temperature NH₃-SCR-DeNO_x and can be monitored by in situ FT-IR and in situ DR UV Vis spectroscopy.

Figure 8 and Figure S11 present the top-down projection of the in situ FT-IR spectra collected for the Cu-containing ERI and SSZ-13 catalysts contacted with reactants for 1 h at 125 °C. In Cu-ERI (Figure 8a), the bands of the Cu²⁺(NO) mononitrosyl (1895 cm⁻¹), N₂O (2224 cm⁻¹) appeared immediately when the NO₃⁻/NO₂⁻ bands (located at 1300, 1395, 1540, and 1600 cm⁻¹) accompanied by the formation of NO⁺ ions (2130 cm⁻¹) started

to dominate the spectrum in the later SCR reaction course. The band at 1624 cm^{-1} can be attributed to ammonia molecules in a coordination sphere of Cu^{2+} ions consumed in favor of the production of nitrates/nitrites. The $\text{Cu}^+(\text{NO})$ species are identified by the 1775 and 1740 cm^{-1} bands. Overall, the most dominant species detected for Cu-ERI, also in the presence of water vapor, are the nitrates (located at 1395 and 1540 cm^{-1}). The different positions of the $\text{Cu}^{2+}(\text{NO})$ mononitrosyls (1900 and 1905 cm^{-1}) formed on the surface of the Cu-ERI_NaOH/2 sample (Figure 8b) compared to Cu-ERI indicate the different nature of Cu^{2+} ions ruled by both their different location in the zeolite framework and the alteration of the ligand in the copper coordination sphere induced by water presence. Nitrates (located at 1300 and 1550 cm^{-1}) also appeared to a limited extent on the surface of Cu-ERI_NaOH/2 than of Cu-ERI. The presence of water vapor in the reaction mixture (Figure S11a,b) influences the SCR reaction that is detected as a decrease in the nitrate concentration (the lack of the bands at 1540 and 1395 cm^{-1}) in favor of water formation (1625 cm^{-1}). We also observed the NH_4^+ species (1425 cm^{-1}), but their amount not being affected during the whole reaction course points to them serving as spectator species under these reaction conditions, despite serving as a reservoir of adsorbed NH_3 at higher temperature SCR stage [46].

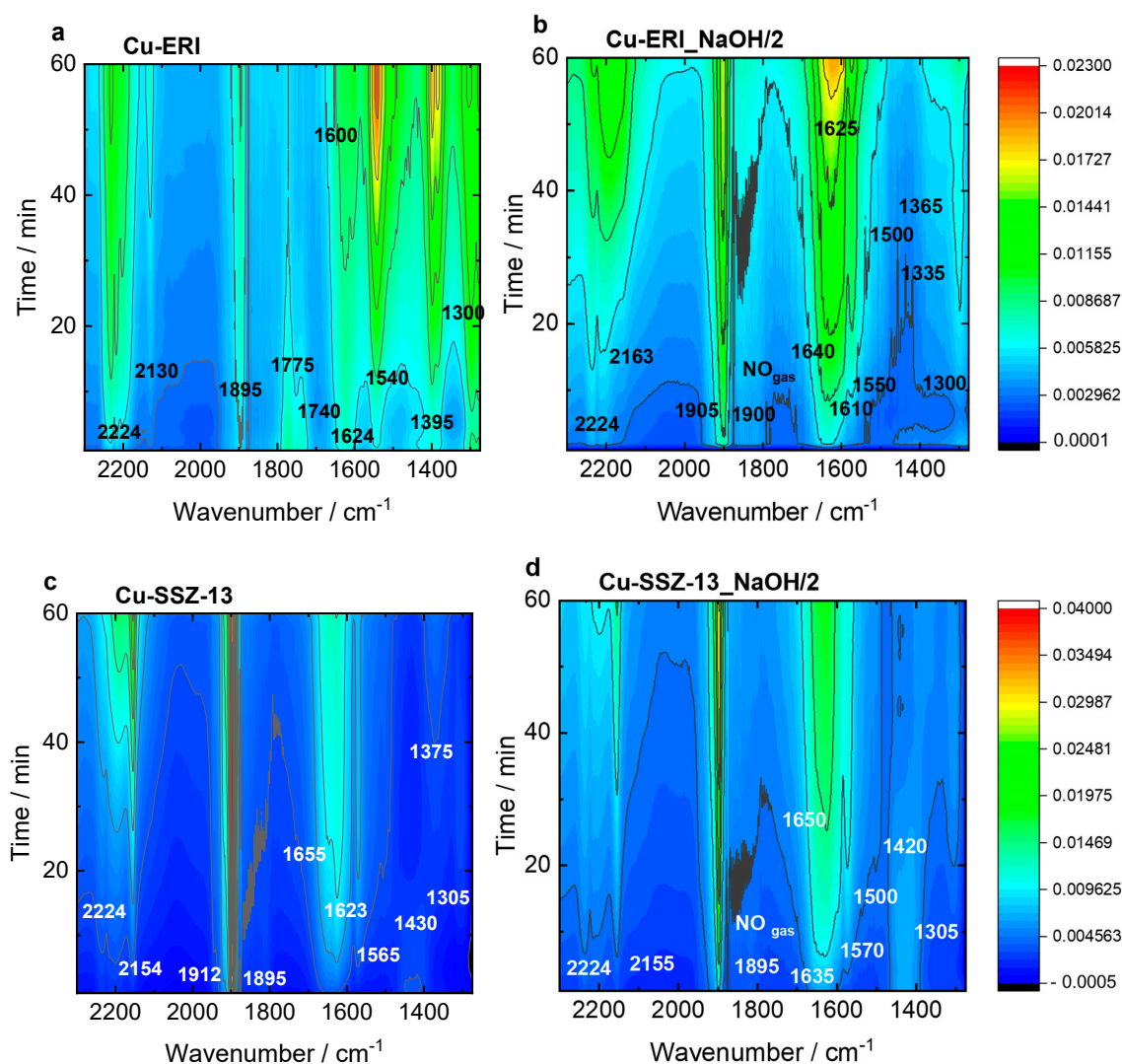


Figure 8. In situ FT-IR spectra of (a,b) Cu-containing ERI and (c,d) Cu-containing SSZ-13 samples, recorded during NH_3 -SCR-De NO_x at $125\text{ }^\circ\text{C}$. Reaction conditions: $m_K = 0.1\text{ g}$, $c(\text{NO}) = 0.1\text{ vol.}\%$, $c(\text{NH}_3) = 0.1\text{ vol.}\%$, $c(\text{O}_2) = 10\text{ vol.}\%$, He balance, $F_{\text{TOT}} = 120\text{ ml min}^{-1}$.

The Cu-SSZ-13 catalyst (Figure 8c) is dominated by the $\text{Cu}^{2+}(\text{NO})$ mononitrosyls (1895 and 1912 cm^{-1}), N_2O (2224 cm^{-1}), and amine Cu^{2+} adducts (1623 cm^{-1}). The latter are converted in water (1655 cm^{-1}) and $\text{NO}_3^-/\text{NO}_2^-$ species (1375 and 1565 cm^{-1}), which is accompanied by the formation of NO^+ ions (2130 cm^{-1}). This weak intensity of nitrates, compared to Cu-ERI, could be indicative of the higher activity of the CHA-based catalysts. Still, the presence of water vapor in the feed mainly results in a decrease in the nitrate and $\text{Cu}^{2+}(\text{NO})$ mononitrosyls (Figure S11c). Regarding the Cu-SSZ-13_NaOH/2 sample (Figure 8d), the water (1650 cm^{-1}), $\text{Cu}^{2+}(\text{NO})$ mononitrosyl (1895 cm^{-1}), and nitrates (1500 and 1570 cm^{-1}) start to be the dominant species. The appearance of NH_4^+ species is also detected (1410 cm^{-1}). They are formed in the first reaction period and then disappear with the depletion of the $\text{Cu}^{2+}\text{-NH}_3$ (1635 cm^{-1}) and nitrates (1570 and 1500 cm^{-1}), indicating their intermediary role in the SCR process. The introduction of water in the gas mixture (Figure S11d) results in changes in the position of the mononitrosyl band (1900 cm^{-1}), as previously detected for the Cu-containing ERI samples. A high number of $\text{NO}_3^-/\text{NO}_2^-$ species (1575 , 1520 , 1350 , 1310 cm^{-1}) is also confirmed. The results suggest the importance of the interplay between the copper sitting at different locations and various hydrothermal stability; thus, $\text{NH}_3\text{-SCR-DeNO}_x$ activity is forced by the zeolite framework type.

Furthermore, the $\text{NH}_3\text{-SCR-DeNO}_x$ over the Cu-containing ERI and SSZ-13 samples was investigated via in situ DR UV-Vis (Figure 9 and Figure S12). The bands previously mentioned related to the oxygen-to-metal charge transfer and d–d transition of Cu^{2+} are visible. However, after the catalysts come into contact with the reaction gases, the d–d transition band experiences a shift to higher wavenumber values from $12,200\text{--}12,600\text{ cm}^{-1}$ to $14,200\text{--}15,300\text{ cm}^{-1}$. This reflects the interaction of NH_3 with copper species. Thus, the d–d transition band no longer belongs to isolated Cu^{2+} but to the copper present in amine complexes (e.g., $[\text{Cu}^{\text{II}}(\text{NH}_3)_4]^+$) [47]. In the further course of the reaction, a new band also appears at $28,200\text{--}28,800\text{ cm}^{-1}$, which is assigned to the $[\text{Cu}^{\text{II}}_2(\text{NH}_3)_4\text{O}_2]^{2+}$ intermediates with a side on the $\mu\text{-}\eta^2,\eta^2\text{-peroxo}$ diammino dicopper(II) structure [46,47]. In the spectra of Cu-containing ERI (Figure 9a,b), the $[\text{Cu}^{\text{II}}_2(\text{NH}_3)_4\text{O}_2]^{2+}$ are clearly visible below $250\text{ }^\circ\text{C}$. For Cu-ERI_NaOH/2, already at $75\text{ }^\circ\text{C}$ a slight band at $28,600\text{ cm}^{-1}$ is present, but the band related to the d–d transition does not shift to higher wavenumbers. The intensity of the strong band at $28,600\text{ cm}^{-1}$ increases between 100 and $125\text{ }^\circ\text{C}$, while at the same time, the d–d transition band shifts to higher wavenumbers (i.e., indicating the presence of diamino dicopper species over this sample). Above $125\text{ }^\circ\text{C}$, the band at $28,600\text{ cm}^{-1}$ decreases in intensity until its disappearance at $250\text{ }^\circ\text{C}$. At progressively higher temperatures, the d–d transition signal returns to the wavenumber values previous to starting the reaction. The difference between $20,000$ and $30,000\text{ cm}^{-1}$ in the activation spectra of Cu-ERI and Cu-ERI_NaOH/2 (arising due to the different nature of copper species in these samples) explains why the band at ca. $28,600\text{ cm}^{-1}$ is more pronounced in Cu-ERI_NaOH/2 than in the other sample.

For Cu-SSZ-13 (Figure 9c), as the reaction mixture comes into contact with the sample already at $75\text{ }^\circ\text{C}$, a strong band appears at $28,200\text{ cm}^{-1}$, and the d–d transition band shifts. At $250\text{ }^\circ\text{C}$, this band disappears, and the d–d transition band returns to its original position. On the contrary, for Cu-SSZ-13-NaOH/2, the bands related to the diamino dicopper complex become visible above $75\text{ }^\circ\text{C}$. Indeed, below $250\text{ }^\circ\text{C}$, Cu-SSZ-13 is more active than Cu-SSZ-13_NaOH/2 for $\text{NH}_3\text{-SCR-DeNO}_x$ (Figure 7). The formation of the $[\text{Cu}^{\text{I}}(\text{NH}_3)_2]^+$ intermediate can be hampered by Cu^{2+} pairs coordinated with two Al sites [48], which are the main species present in the Cu-SSZ-13_NaOH/2 sample. Above $250\text{ }^\circ\text{C}$, the solvation shell of ammonia around the copper cations is not stable [49], indicating that a different reaction mechanism is dominant at high temperatures [3,50,51].

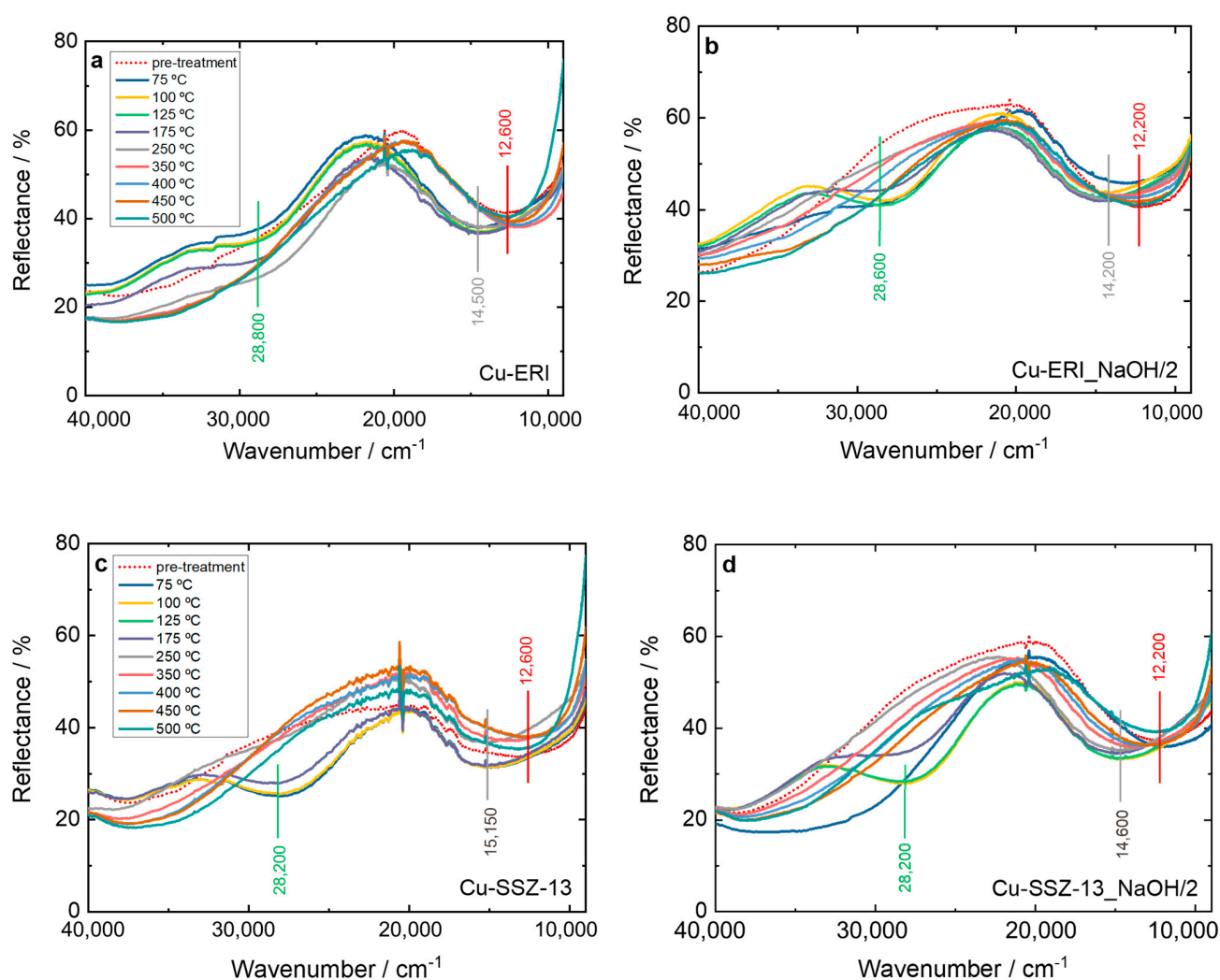


Figure 9. In situ DR UV-Vis DR spectrum of (a,b) Cu-containing ERI and (c,d) Cu-containing SSZ-13 samples during NH_3 -SCR- DeNO_x at different temperatures. Reaction conditions: $m_K = 0.1$ g, $c(\text{NO}) = 0.1$ vol.-%, $c(\text{NH}_3) = 0.1$ vol.-%, $c(\text{O}_2) = 10$ vol.-%, He balance, $F_{\text{TOT}} = 120$ ml min^{-1} ; (a–d) sample labels are identical.

Furthermore, we investigated the influence of 5 vol.% H_2O on forming the reaction intermediates. However, both Cu-containing ERI samples exhibit similar behavior in the absence of water (Figures 9a,b and S12a,b). This aligns with the results of catalytic studies (Figure S9b), which do not show any significant differences in NO conversion among these samples. Regarding the Cu-containing SSZ-13 samples under wet conditions (Figure S12c,d), the band at $28,800$ cm^{-1} recedes slowly below 250 $^\circ\text{C}$, which could indicate that the reduction of the complex is slower than in the absence of water. At high temperatures (>350 $^\circ\text{C}$), the vertical asymptote present at low wavenumber range is caused by spurious black-body radiation emitted by the heating device.

The Cu-ERI_NaOH/2 and Cu-SSZ-13_NaOH/2 samples were also investigated for NH_3 oxidation. The spectra recorded for both samples (Figure S13) are characteristic of the conventional activation of Cu-containing zeolites under an O_2 atmosphere [46]. No appearance of the band related to the diammino dicopper intermediates was found. In contrast, the structure of the d–d transition band is less resolved, which is unrelated to the reaction. Indeed, NO molecules are necessary to activate the copper ammine complexes that precede the diammino dicopper complex [52].

4. Experimental

4.1. Catalyst Preparation

Briefly, 1 g of calcined zeolite (550 °C for 4 h in static air, 1 °C min⁻¹) per 100 mL of aqueous solution of HNO₃ (65 wt.%, Merck, Darmstadt, Germany) or NaOH (≥97 wt.%, Merck, Darmstadt, Germany) was stirred for 0.5–2 h at 65 °C under reflux. After treatment, the solution was cooled down in a water bath, and subsequently, the sample was thoroughly washed with distilled water. After drying, the resulting materials were transformed into their protonic form by three-fold ion exchange with an aqueous solution (0.5 M) of ammonium nitrate (>99 wt.%, Merck, Darmstadt, Germany) at 60 °C for 1 h. After filtration, washing, and drying, they were calcined at 550 °C for 4 h in static air (heating rate of 1 °C min⁻¹).

Subsequently, the materials were subjected to ion exchange in an aqueous solution of (0.05 M) copper acetate (Cu(OOCCH₃)₂, ≥98 wt.%, Alfa Aesar, Karlsruhe, Germany) for 24 h at room temperature. After the ion exchange, the resulting product was separated through filtration and then extensively washed. The obtained materials were subsequently dried at room temperature. Finally, the solids were calcined at 550 °C for 4 h in static air (heating rate of 1 °C min⁻¹).

4.2. Catalyst Characterization, Catalytic Experiments, and In Situ Investigations

The physico-chemical characterization of the ERI- and SSZ-13-based samples, as well as their copper-containing forms, was performed by applying the XRD, NMR, N₂ sorption, ICP-OES, NH₃-TPD, H₂-TPR, DR UV-Vis, X-ray absorption spectroscopy (XAS), EPR, and temperature-programmed isotopic exchange (TPIE) techniques. Subsequently, the associated catalytic activity and N₂ selectivity were investigated over Cu-containing ERI and SSZ-13 samples for NH₃-SCR-DeNO_x and NH₃-SCO, including in situ FT-IR and DR UV-Vis. The details of the experimental procedures can be found in the Supplementary Materials.

5. Conclusions

The post-synthetic modifications applied to the ERI and SSZ-13 zeolites have influenced both the physico-chemical properties and the activity of the corresponding catalysts. The modification of the ERI zeolite (with an aqueous solution of 0.2 M NaOH for 2 h) led to enhanced activity up to 500 °C of Cu-ERI_NaOH/2 compared to Cu-ERI. Otherwise, the micro-/mesoporous Cu-SSZ-13_NaOH/2 exhibits a lower catalytic activity than the conventional Cu-SSZ-13. Characterization methods such as H₂-TPR have provided insight into how the zeolite modifications affected the copper species present in the samples. In the case of the Cu-containing ERI catalysts, the basic leaching prevented the formation of aggregated copper species, which are active for the NH₃-SCO. For Cu-containing SSZ-13, the amount of Cu²⁺ coordinated with one Al site, and [Cu(OH)]⁺ is reduced for the post-modified zeolite-based sample, thus reducing the material's catalytic activity. In situ FT-IR provides evidence of the formation of copper nitrates, while in situ DR UV-Vis revealed the formation of μ-η²,η²-peroxo dicopper(II) intermediates. The enhanced activity of Cu-SSZ-13 is correlated with the more significant reduction of Cu nitrates and its superior ability to generate Cu dimer species in the reaction. The reduction of Cu dimer species is hampered in the presence of H₂O in the feed, resulting in the lower low-temperature activity of Cu-containing SSZ-13 samples.

Supplementary Materials: The following supporting information can be downloaded at: <https://www.mdpi.com/article/10.3390/catal14070457/s1>, Figure S1: XRD patterns of the parent and post-modified form of (a) ERI and (b) SSZ-13 samples. Figure S2: (a,b) N₂ sorption isotherms collected at −196 °C and c,d) BJH pore width distribution of ERI, SSZ-13 samples; (a,c) and (b,d) sample labels are identical. Figure S3: (a) Contribution of different Si coordination to the area of the ²⁹Si NMR spectra of Cu-containing ERI and SSZ-13 samples and (b) a schematic diagram of the coordination environment of Si and Al. Figure S4: Results of the TPD-NH₃ over (a) Cu-containing ERI and (b) SSZ-13 samples. Figure S5: Deconvoluted H₂-TPR profiles of (a) Cu-containing ERI and (b) Cu-containing SSZ-13 samples. Figure S6: EPR spectra of the hydrated Cu-containing

ERI and SSZ-13 samples recorded at $-196\text{ }^{\circ}\text{C}$. Figure S7: (a,b) XANES spectra of Cu-containing zeolite samples with copper references, (a) and (b) sample labels are identical. Figure S8: Results of the TPIE experiment obtained for (a) Cu-ERI_NaOH/2 and (b) Cu-SSZ-13_NaOH/2. Figure S9: NO conversion of the Cu-containing ERI and SSZ-13 samples: (a,c) without H_2O in the feed, (b,d) in the presence of H_2O in the feed. Reaction conditions: $m_K = 0.1\text{ g}$, $c(\text{NO}) = 0.05\text{ vol.-%}$, $c(\text{NH}_3) = 0.0575\text{ vol.-%}$, $c(\text{O}_2) = 4\text{ vol.-%}$, ($c(\text{H}_2\text{O}) = 5\text{ vol.-%}$ when used), He balance, $F_{\text{TOT}} = 120\text{ ml min}^{-1}$, $\text{GHSV} = 30,000\text{ h}^{-1}$. Figure S10: a) NO conversion of Cu-containing SSZ-13 sample (based on support modified with a 0.1 M NaOH solution) and (b) NH_3 conversion*. Reaction conditions: $m_K = 0.1\text{ g}$, $c(\text{NO}) = 0.05\text{ vol.-%}$, $c(\text{NH}_3) = 0.0575\text{ vol.-%}$, $c(\text{O}_2) = 4\text{ vol.-%}$, ($c(\text{H}_2\text{O}) = 5\text{ vol.-%}$ when used), He balance, $F_{\text{TOT}} = 120\text{ ml min}^{-1}$, $\text{GHSV} = 30,000\text{ h}^{-1}$. *Reaction conditions: $m_K = 0.1\text{ g}$, $c(\text{NH}_3) = 0.1\text{ vol.-%}$, $c(\text{O}_2) = 10\text{ vol.-%}$, He balance, $F_{\text{TOT}} = 120\text{ ml min}^{-1}$, $\text{GHSV} = 30,000\text{ h}^{-1}$. Figure S11: In situ FT-IR spectra of (a,b) Cu-containing ERI and (c,d) Cu-containing SSZ-13 samples, recorded during $\text{NH}_3\text{-SCR-DeNO}_x$ at $125\text{ }^{\circ}\text{C}$. Reaction conditions: $m_K = 0.1\text{ g}$, $c(\text{NO}) = 0.1\text{ vol.-%}$, $c(\text{NH}_3) = 0.1\text{ vol.-%}$, $c(\text{O}_2) = 10\text{ vol.-%}$, $c(\text{H}_2\text{O}) = 5\text{ vol.-%}$, He balance, $F_{\text{TOT}} = 120\text{ ml min}^{-1}$. Figure S12: In situ DR UV-Vis DR spectrum of (a,b) Cu-containing ERI and (c,d) Cu-containing SSZ-13 samples during $\text{NH}_3\text{-SCR-DeNO}_x$ at different temperatures. Reaction conditions: $m_K = 0.1\text{ g}$, $c(\text{NO}) = 0.1\text{ vol.-%}$, $c(\text{NH}_3) = 0.1\text{ vol.-%}$, $c(\text{O}_2) = 10\text{ vol.-%}$, $c(\text{H}_2\text{O}) = 5\text{ vol.-%}$, He balance, $F_{\text{TOT}} = 120\text{ ml min}^{-1}$; (a,b) and (c,d) sample labels are identical. Figure S13: In situ DR UV-Vis spectrum of (a) Cu-ERI_NaOH/2, and (b) Cu-SSZ-13_NaOH/2 applied to the $\text{NH}_3\text{-SCO}$ at different temperatures. Reaction conditions: $m_K = 0.1\text{ g}$, $c(\text{NH}_3) = 1000\text{ ppm}$, $c(\text{O}_2) = 10\text{ vol.-%}$, He balance, $F_{\text{TOT}} = 120\text{ ml min}^{-1}$. Table S1: The results of the textural properties of the parent and post-modified form of ERI, SSZ-13 samples: specific surface area ($A_{s(\text{BET})}$), micropore pore volume ($V_{(\text{MIC})}$), mesopore pore volume ($V_{(\text{MES})}$), total pore volume ($V_{(\text{TOT})}$) and average pore width (d_{WP}). Table S2: Deconvolution of the ^{29}Si MAS NMR spectra. Table S3: Deconvolution of the ^{27}Al MAS NMR spectra. Table S4: Contribution of the different peaks after deconvolution of $\text{H}_2\text{-TPR}$ profiles. Table S5: Spin Hamiltonian parameters used for spectral simulation of Cu-containing zeolite samples before and after activation at $300\text{ }^{\circ}\text{C}$ for 1 h under vacuum. Table S6: Composition in percentage for different Cu species in activated Cu-containing zeolite samples obtained from the spectral simulations using EasySpin.

Author Contributions: A.M.R.: Investigation, data curation, software, writing—original draft, writing—review and editing. G.D.: Investigation, data curation. K.G.-M.: Investigation, data curation, writing—review and editing. M.R.: Investigation, data curation. A.W.: Investigation, data curation, writing—review and editing. M.F.L.: Investigation, data curation, writing—review and editing. M.B.: Investigation, data curation. M.S.: Investigation, data curation. S.B.: Review. A.P. Review. R.G.: Review. M.J.: Conceptualization, methodology, investigation, data curation, data management, writing—original draft, writing—review and editing, supervision, visualization, project management. All authors have read and agreed to the published version of the manuscript.

Funding: M.J. acknowledges a DFG Research Grant JA 2998/2-1. M.F.L. acknowledges a DFG Research Grant of GRK:2721. K.G.M. acknowledges the Grant No. 2021/41/B/ST4/00048 from the National Science Centre, Poland. G.D., M.S. and S.B. acknowledge support from the Project CH4.0 under the MUR program “Dipartimenti di Eccellenza 2023–2027” (CUP: D13C22003520001).

Data Availability Statement: Data are contained within the article and Supplementary Materials.

Conflicts of Interest: The authors declare no conflict of interest.

References

1. Molokova, A.Y.; Borfecchia, B.; Martini, A.; Pankin, I.A.; Atzori, C.; Mathon, O.; Bordiga, S.; Wen, F.; Vennestrøm, P.N.R.; Berlier, G.; et al. SO_2 poisoning of Cu-CHA deNO_x catalyst: The most vulnerable Cu species identified by X-ray absorption spectroscopy. *JACS Au* **2022**, *2*, 787–792. [[CrossRef](#)] [[PubMed](#)]
2. Zhao, J.; Chen, Y.; Wang, Y.; Li, Z.; Nkinahamira, F.; Zhu, R.; Zhang, J.; Sun, S.; Zhu, Y.; Li, H.; et al. The poisoning mechanism of $\text{H}_2\text{O}/\text{SO}_2$ to In/H-Beta for selective catalytic reduction of NO_x with methane. *Appl. Catal. A, Gen.* **2023**, *649*, 118973. [[CrossRef](#)]
3. Jabłońska, M. Review of the application of Cu-containing SSZ-13 in $\text{NH}_3\text{-SCR-DeNO}_x$ and $\text{NH}_3\text{-SCO}$. *RSC Adv.* **2022**, *12*, 25240–25261. [[CrossRef](#)] [[PubMed](#)]
4. Wang, J.; Zhao, H.; Haller, G.; Li, Y. Recent advances in the selective catalytic reduction of NO_x with NH_3 on Cu-chabazite catalysts. *Appl. Catal. B Environ.* **2017**, *202*, 346–354. [[CrossRef](#)]

5. Salazar, M.; Hoffmann, S.; Tillmann, L.; Singer, V.; Becker, R.; Grünert, W. Hybrid catalysts for the selective catalytic reduction (SCR) of NO by NH₃: Precipitates and physical mixtures. *Appl. Catal. B Environ.* **2017**, *218*, 793–802. [[CrossRef](#)]
6. Shi, Z.; Peng, Q.; Jiaqiang, E.; Xie, B.; Wei, J.; Yin, R.; Fu, G. Mechanism, performance and modification methods for NH₃-SCR catalysts: A review. *Fuel* **2023**, *331*, 125885. [[CrossRef](#)]
7. Zhu, J.; Liu, Z.; Xu, L.; Ohnishi, T.; Yanaba, Y.; Ogura, M.; Wakihara, T.; Okubo, T. Understanding the high hydrothermal stability and NH₃-SCR activity of the fast-synthesized ERI zeolite. *J. Catal.* **2020**, *391*, 346–356. [[CrossRef](#)]
8. Sultana, A.; Nanba, T.; Sasaki, M.; Haneda, M.; Suzuki, K.; Hamada, H. Selective catalytic reduction of NO_x with NH₃ over different copper exchanged zeolites in the presence of decane. *Catal. Today* **2011**, *164*, 495–499. [[CrossRef](#)]
9. Liu, J.; Yu, F.; Liu, J.; Cui, L.; Zhao, Z.; Wei, Y.; Sun, Q. Synthesis and kinetics investigation of meso-microporous Cu-SAPO-34 catalysts for the selective catalytic reduction of NO with ammonia. *J. Environ. Sci.* **2016**, *48*, 45–58. [[CrossRef](#)]
10. Rutkowska, M.; Pacia, I.; Basag, S.; Kowalczyk, A.; Piwowarska, Z.; Duda, M.; Tarach, K.A.; Góra-Marek, K.; Michalik, M.; Díaz, U.; et al. Catalytic performance of commercial Cu-ZSM-5 zeolite modified by desilication in NH₃-SCR and NH₃-SCO processes. *Microporous Mesoporous Mater.* **2017**, *246*, 193–206. [[CrossRef](#)]
11. Góra-Marek, K.; Brylewska, K.; Tarach, K.A.; Rutkowska, M.; Jabłońska, M.; Choi, M.; Chmielarz, L. IR studies of Fe modified ZSM-5 zeolites of diverse mesopore topologies in the terms of their catalytic performance in NH₃-SCR and NH₃-SCO processes. *Appl. Catal. B Environ.* **2015**, *179*, 589–598. [[CrossRef](#)]
12. Oord, R.; Ten Have, I.C.; Arends, J.M.; Hendriks, F.C.; Schmidt, J.; Lezcano-Gonzalez, I.; Weckhuysen, B.M. Enhanced activity of desilicated Cu-SSZ-13 for the selective catalytic reduction of NO_x and its comparison with steamed Cu-SSZ-13. *Catal. Sci. Technol.* **2017**, *7*, 3851–3862. [[CrossRef](#)]
13. Wu, G.; Liu, S.; Chen, Z.; Yu, Q.; Chu, Y.; Xiao, H.; Peng, H.; Fang, D.; Deng, S.; Chen, Y. Promotion effect of alkaline leaching on the catalytic performance over Cu/Fe-SSZ-13 catalyst for selective catalytic reduction of NO_x with NH₃. *J. Taiwan Inst. Chem. Eng.* **2022**, *134*, 104355. [[CrossRef](#)]
14. Jabłońska, M.; Góra-Marek, K.; Grilc, M.; Bruzzese, P.C.; Poppitz, D.; Pyra, K.; Liebau, M.; Pöppel, A.; Likozar, B.; Gläser, R. Effect of textural properties and presence of co-cation on NH₃-SCR activity of Cu-exchanged ZSM-5. *Catalysts* **2021**, *11*, 843. [[CrossRef](#)]
15. Suharbiansah, R.S.R.; Pyra, K.; Liebau, M.; Poppitz, D.; Góra-Marek, K.; Gläser, R.; Jabłońska, M. Micro-/mesoporous copper-containing zeolite Y applied in NH₃-SCR, DeNO_x. *Microporous Mesoporous Mater.* **2022**, *334*, 111793. [[CrossRef](#)]
16. Tekla, J.; Lakiss, L.; Valchev, V.; Tarach, K.A.; Jabłońska, M.; Girman, V.; Szymocha, A.; Kowalczyk, A.; Góra-Marek, K.; Gilson, J.-P. Increasing the catalytic performance of erionite by hierarchization. *Microporous Mesoporous Mater.* **2020**, *299*, 110088. [[CrossRef](#)]
17. Akgul, F.A.; Akgul, G.; Yildirim, N.; Unalan, H.E.; Turan, R. Influence of thermal annealing on microstructural, morphological, optical properties and surface electronic structure of copper oxide thin films. *Mater. Chem. Phys.* **2014**, *147*, 987–995. [[CrossRef](#)]
18. Thommes, M.; Kaneko, K.; Neimark, A.V.; Olivier, J.P.; Rodriguez-Reinoso, F.; Rouquerol, J.; Sing, K.S.W. Physisorption of gases, with special reference to the evaluation of surface area and pore size distribution (IUPAC Technical Report). *Pure Appl. Chem.* **2015**, *87*, 1051–1069. [[CrossRef](#)]
19. Sommer, L.; Mores, D.; Svelle, S.; Stöcker, M.; Weckhuysen, B.M.; Olsbye, U. Mesopore formation in zeolite H-SSZ-13 by desilication with NaOH. *Microporous Mesoporous Mater.* **2010**, *132*, 384–394. [[CrossRef](#)]
20. Lillerud, K.P. Aluminium distribution in the zeolites offretite and erionite. *Zeolites* **1987**, *7*, 14–17. [[CrossRef](#)]
21. Occelli, M.L.; Ritz, G.P.; Iyer, P.S.; Walker, R.D.; Gerstein, B.C. Quarternary ammonium cation effects on the crystallization of zeolites of the offretite-erionite family: Part III. 29Si nmr, 27Al nmr, and mid-ir characterization. *Zeolites* **1989**, *9*, 104–110.
22. Lusardi, M.; Chen, T.T.; Kale, M.; Kang, J.H.; Neurock, M.; Davis, M.E. Carbonylation of dimethyl ether to methyl acetate over SSZ-13. *ACS Catal.* **2019**, *10*, 842–851. [[CrossRef](#)]
23. Bing, L.; Liu, J.; Yi, K.; Li, F.; Han, D.; Wang, F.; Wang, G. Rapid synthesis of hierarchical SSZ-13 zeolite microspheres via a fluoride-assisted in situ growth route using aluminum isopropoxide as aluminum source. *RSC Adv.* **2020**, *10*, 3566–3571. [[CrossRef](#)]
24. Villamaina, R.; Liu, S.; Nova, I.; Tronconi, E.; Ruggeri, M.P.; Collier, J.; York, A.; Thompsett, D. Speciation of Cu cations in Cu-CHA catalysts for NH₃-SCR: Effects of SiO₂/AlO₃ ratio and Cu-loading investigated by transient response methods. *ACS Catal.* **2019**, *9*, 8916–8927. [[CrossRef](#)]
25. Hu, W.; Selleri, T.; Gramigni, F.; Fenes, E.; Rout, K.R.; Liu, S.; Nova, I.; Chen, D.; Gao, X.; Tronconi, E. On the redox mechanism of low-temperature NH₃-SCR over Cu-CHA: A combined experimental and theoretical study of the reduction half cycle. *Angew. Chem. Int. Ed.* **2021**, *60*, 7197–7204. [[CrossRef](#)]
26. Wang, H.; Xu, R.; Jin, Y.; Zhang, R. Zeolite structure effects on Cu active center, SCR performance and stability of Cu-zeolite catalysts. *Catal. Today* **2019**, *327*, 295–307. [[CrossRef](#)]
27. Jabłońska, M.; Góra-Marek, K.; Bruzzese, P.C.; Palčić, A.; Pyra, K.; Tarach, K.; Bertmer, M.; Poppitz, D.; Pöppel, A.; Gläser, R. Influence of framework n(Si)/n(Al) ratio on the nature of Cu species in Cu-ZSM-5 for NH₃-SCR-DeNO_x. *ChemCatChem* **2022**, *14*, e202200627. [[CrossRef](#)]
28. Suharbiansah, R.S.R.; Lukman, M.F.; Nannuzzi, C.; Wach, A.; Góra-Marek, K.; Liebau, M.; Palčić, A.; Pöppel, A.; Berlier, G.; Bordiga, S.; et al. Effect of the preparation method on the catalytic properties of copper-containing zeolite Y applied for NH₃-SCR-DeNO_x. *Catal. Sci. Technol.* **2023**, *13*, 3804–3817. [[CrossRef](#)]

29. Jabłońska, M.; Góra-Marek, K.; Lukman, M.F.; Tarach, K.; Bertmer, M.; Denecke, R.; Poppitz, D.; Marcinowski, K.; Pöpl, A.; Gläser, R. Selective catalytic reduction of NO_x over micro-/meso-/macroporous Cu-SAPO-34. *Catal. Sci. Technol.* **2022**, *12*, 6660–6675. [[CrossRef](#)]
30. Godiksen, A.; Vennestrøm, P.N.R.; Rasmussen, S.B.; Mossin, S. Identification and quantification of copper sites in zeolites by electron paramagnetic resonance spectroscopy. *Top. Catal.* **2017**, *60*, 13–29. [[CrossRef](#)]
31. Stoll, S.; Schweiger, A. EasySpin, a comprehensive software package for spectral simulation and analysis in EPR. *J. Magn. Reson.* **2006**, *178*, 42–55. [[CrossRef](#)]
32. Zamadics, M.; Kevan, L. Electron spin resonance and electron spin echo modulation studies of copper (II) ions in the aluminosilicate chabazite: A comparison of copper (II) cation location and adsorbate interaction with isostructural silicoaluminophosphate-34. *J. Phys. Chem.* **1992**, *96*, 8989–8993. [[CrossRef](#)]
33. Fernández, E.; Moreno-González, M.; Moliner, M.; Blasco, T.; Boronat, M.; Corma, A. Modeling of EPR parameters for Cu (II): Application to the selective reduction of NO_x catalyzed by Cu-zeolites. *Top. Catal.* **2018**, *61*, 810–832. [[CrossRef](#)]
34. Larsen, S.C.; Aylor, A.; Bell, A.T.; Reimer, J.A. Electron paramagnetic resonance studies of copper ion-exchanged ZSM-5. *J. Phys. Chem.* **1994**, *98*, 11533–11540. [[CrossRef](#)]
35. Alayon, E.M.C.; Nachtegaal, M.; Bodi, A.; van Bokhoven, J.A. Reaction conditions of methane-to-methanol conversion affect the structure of active copper sites. *ACS Catal.* **2014**, *4*, 16–22. [[CrossRef](#)]
36. Martini, A.; Alladio, E.; Borfecchia, E. Determining Cu-speciation in the Cu-CHA zeolite catalyst: The potential of multivariate curve resolution analysis of in situ XAS data. *Top. Catal.* **2018**, *61*, 1396–1407. [[CrossRef](#)]
37. Wang, H.; Jia, J.; Liu, S.; Chen, H.; Wei, Y.; Wang, Z.; Zheng, L.; Wang, Z.; Zhang, R. Highly efficient NO abatement over Cu-ZSM-5 with special nanosheet features. *Environ. Sci. Technol.* **2021**, *55*, 5422–5434. [[CrossRef](#)]
38. Borfecchia, E.; Lomachenko, K.A.; Giordanino, F.; Falsig, H.; Beato, P.; Soldatov, A.V.; Bordiga, S.; Lamberti, C. Revisiting the nature of Cu sites in the activated Cu-SSZ-13 catalyst for SCR reaction. *Chem. Sci.* **2015**, *6*, 548–563. [[CrossRef](#)]
39. Persson, I.; Lundberg, D.; Bajnóczi, E.G.; Klementiev, K.; Just, J.; Sigfridsson Clauss, K.G. V EXAFS study on the coordination chemistry of the solvated copper (II) ion in a series of oxygen donor solvents. *Inorg. Chem.* **2020**, *59*, 9538–9550. [[CrossRef](#)] [[PubMed](#)]
40. Chillemi, G.; Pace, E.; D’Abramo, M.; Benfatto, M. Equilibrium between 5-and 6-fold coordination in the first hydration shell of Cu (II). *J. Phys. Chem. A* **2016**, *120*, 3958–3965. [[CrossRef](#)] [[PubMed](#)]
41. Kwak, J.H.; Tran, D.; Burton, S.D.; Szanyi, J.; Lee, J.H.; Peden, C.H.F. Effects of hydrothermal aging on NH₃-SCR reaction over Cu/zeolites. *J. Catal.* **2012**, *287*, 203–209. [[CrossRef](#)]
42. Zhang, T.; Qiu, F.; Li, J. Design and synthesis of core-shell structured meso-Cu-SSZ-13@ mesoporous aluminosilicate catalyst for SCR of NO_x with NH₃: Enhancement of activity, hydrothermal stability and propene poisoning resistance. *Appl. Catal. B Environ.* **2016**, *195*, 48–58. [[CrossRef](#)]
43. Olsson, L.; Sjövall, H.; Blint, R.J. A kinetic model for ammonia selective catalytic reduction over Cu-ZSM-5. *Appl. Catal. B Environ.* **2008**, *81*, 203–217. [[CrossRef](#)]
44. Gao, F.; Washton, N.M.; Wang, Y.; Kollár, M.; Szanyi, J.; Peden, C.H.F. Effects of Si/Al ratio on Cu/SSZ-13 NH₃-SCR catalysts: Implications for the active Cu species and the roles of Brønsted acidity. *J. Catal.* **2015**, *331*, 25–38. [[CrossRef](#)]
45. Signorile, M.; Borfecchia, E.; Bordiga, S.; Berlier, G. Influence of ion mobility on the redox and catalytic properties of Cu ions in zeolites. *Chem. Sci.* **2022**, *13*, 10238–10250. [[CrossRef](#)] [[PubMed](#)]
46. Fedyna, M.; Mozgawa, B.; Zasada, F.; Góra-Marek, K.; Gryboś, J.; Piskorz, W.; Yin, C.; Zhao, Z.; Pietrzyk, P.; Sojka, Z. Mechanistic stages of the SCR reaction—Insights into the trade-off between NO reduction and NH₃ oxidation over CuSSZ-13 catalysts via isotopic ¹⁵NH₃ and ¹⁸O₂ TPSR and steady state studies supported by IR 2D COS and DFT modeling. *Appl. Catal. B Environ.* **2023**, *325*, 122309. [[CrossRef](#)]
47. Oda, A.; Shionoya, H.; Hotta, Y.; Takewaki, T.; Sawabe, K.; Satsuma, A. Spectroscopic evidence of efficient generation of dicopper intermediate in selective catalytic reduction of NO over Cu-ion-exchanged zeolites. *ACS Catal.* **2020**, *10*, 12333–12339. [[CrossRef](#)]
48. Negri, C.; Sella, T.; Borfecchia, E.; Martini, A.; Lomachenko, K.A.; Janssens, T.V.W.; Cutini, M.; Bordiga, S.; Berlier, G. Structure and reactivity of oxygen-bridged diamino dicopper (II) complexes in Cu-ion-exchanged chabazite catalyst for NH₃-mediated selective catalytic reduction. *J. Am. Chem. Soc.* **2020**, *142*, 15884–15896. [[CrossRef](#)] [[PubMed](#)]
49. Paolucci, C.; Khurana, I.; Parekh, A.A.; Li, S.; Shih, A.J.; Li, H.; Di Iorio, J.R.; Albarracín-Caballero, J.D.; Yezerets, A.; Miller, J.T.; et al. Dynamic multinuclear sites formed by mobilized copper ions in NO_x selective catalytic reduction. *Science* **2017**, *357*, 898–903. [[CrossRef](#)]
50. Gao, F.; Walter, E.D.; Kollar, M.; Wang, Y.; Szanyi, J.; Peden, C.H.F. Understanding ammonia selective catalytic reduction kinetics over Cu/SSZ-13 from motion of the Cu ions. *J. Catal.* **2014**, *319*, 1–14. [[CrossRef](#)]

51. Jabłońska, M. Recent progress in the selective catalytic reduction of NO_x with NH₃ on Cu-SAPO-34 catalysts. *Mol. Catal.* **2022**, *518*, 112111. [[CrossRef](#)]
52. Tarach, K.A.; Jabłońska, M.; Pyra, K.; Liebau, M.; Reiprich, B.; Gläser, R.; Góra-Marek, K. Effect of zeolite topology on NH₃-SCR activity and stability of Cu-exchanged zeolites. *Appl. Catal. B Environ.* **2021**, *284*, 119752. [[CrossRef](#)]

Disclaimer/Publisher's Note: The statements, opinions and data contained in all publications are solely those of the individual author(s) and contributor(s) and not of MDPI and/or the editor(s). MDPI and/or the editor(s) disclaim responsibility for any injury to people or property resulting from any ideas, methods, instructions or products referred to in the content.